Available online at www.sciencedirect.com
ScienceDirect
Trans. Nonferrous Met. Soc. China 35(2025) 2421−2434
Transactions of Nonferrous Metals Society of China
www.tnmsc.cn

Efficient direct regeneration of spent $LiFePO_4$ by low-temperature sintering

Hong-lei SONG[1,2], Zhi-xing WANG[1,2,3], Xin-hai LI[1,2,3], Hua-jun GUO[1,2,3], Wen-jie PENG[1,2], Zhi-liang YAN[4], Cheng-hui ZHENG[4], Jian-qiu LI[4], Jie-xi WANG[1,2,3], Guo-chun YAN[1,2,3]

1. School of Metallurgy & Environment, Central South University, Changsha 410083, China;
2. Engineering Research Center of the Ministry of Education for Advanced Battery Materials, Central South University, Changsha 410083, China;
3. Hunan Provincial Key Laboratory of Nonferrous Value-added Metallurgy, Central South University, Changsha 410083, China;
4. Fujian Evergreen New Energy Technology Co., Ltd., Longyan 364200, China

Received 18 December 2023; accepted 28 June 2024

Abstract: The morphology, crystal structure, and electrochemical performance of spent $LiFePO_4$ (S-LFP) are recovered by one-step low-temperature solid phase sintering. After sintering at 550 °C for 3 h, the secondary particle size distribution of regenerated $LiFePO_4$ (R-LFP) becomes narrower, and the D_{50} is reduced from 5.6 to 2.3 μm. In addition, the content of Li−Fe antisite defect is reduced from 5.73% to 1.20%, and the F is doped to O(2) site in the structure of R-LFP. Moreover, a coating layer comprising carbon and LiF is formed on the surface of R-LFP because of the decomposition of PVDF. Therefore, the R-LFP demonstrates exceptional Li^+ diffusion dynamics and conductivity, which delivers a high discharge capacity of 157.3 mA·h/g at 0.1*C*. And it maintains 92% of its initial capacity after 500 cycles at 1*C*.

Key words: spent $LiFePO_4$; low-temperature sintering; direct regeneration; high-value utilization

1 Introduction

Lithium-ion batteries (LIBs) are widely used in electric vehicles (EVs) and electrochemical energy storage because of their high energy density, high power density, and long life [1−4]. As EVs are one of the important solutions to achieve a carbon-neutral economy [5,6], it is predicted that the total number of EVs on the world's road will reach 253 million by 2030 [7]. In China, the output of lithium iron phosphate (LFP) based batteries reached 332.4 GW·h in 2022, surpassing 212.5 GW·h of ternary lithium-ion batteries. Generally, power batteries have a life span of 7−8 years and are poised for a large-scale retirement in the near future, especially LFP batteries [8]. Spent $LiFePO_4$ (S-LFP) batteries contain a variety of flammable fluorine-containing organic electrolytes, which will cause safety and environmental pollution problems if not properly treated [9]. In addition, the scrap ratio of electrode pieces accounts for 8% in battery manufacturing due to the production efficiency limit, leading to the fact that spent scraps are one of the major sources of S-LFP. Specifically, there should be 160000 t LFP scraps based on the output of LFP production in China (~2 million tons). Generally, the content of Li element in S-LFP is 5−7 wt.%, which is much higher than that in natural ore [10]. Therefore, recycling S-LFP batteries can

Corresponding author: Guo-chun YAN, Tel: +86-15273163234, E-mail: happyygc@csu.edu.cn
https://doi.org/10.1016/S1003-6326(25)66824-5

not only solve the problems of environmental pollution, but also realize the recycling of strategic metal Li, which will bring high economic value.

The recovery of S-LFP cathode materials includes pyrometallurgy, hydrometallurgy, bio-metallurgy, and direct regeneration [10−16]. Pyro-metallurgy is easy to realize industrialization, but the reaction needs to be performed at high temperature. High energy consumption and equipment corrosion are long-standing problems. Hydrometallurgy has the advantages of high leaching rate and good selectivity, but it consumes plenty of acid, alkali, and oxidant, producing massive secondary waste (Na_2SO_4, and Na_3PO_3, etc). This is unfavorable for the S-LFP with low economic value except for Li. Bioleaching is a less energy-intensive and less polluting process. However, its industrial application has been limited by slow leaching rates under kinetic conditions [14]. Therefore, pyrometallurgy, hydrometallurgy, and biometallurgy methods may not be the best for the LFP scraps from electrode pieces and battery manufacturing processes.

Direct regeneration can repair the lattice defects and Li vacancies of the S-LFP by supplementing Li in the liquid or solid phase, to restore the electrochemical performance [17,18]. LI et al [17] repaired S-LFP by supplementing Li_2CO_3 and sintering at 650 °C for 1 h in Ar+H_2 mixed atmosphere. The peak intensity of $FePO_4$ and P_2O_5 impurity phases in the regenerated $LiFePO_4$ (R-LFP) was weakened, and the initial discharge capacity reached 147.3 mA·h/g at 0.2*C*. To reduce energy consumption, XU et al [18] carried out aqueous relithiation of S-LFP at a lower temperature. Li supplementation of S-LFP was achieved at 70 °C and 60 °C for 10 h and 17 h, respectively, and then the S-LFP was regenerated at 600 °C for 2 h. The discharge capacity of R-LFP was 159 mA·h/g at 0.5*C*, and the capacity retention was more than 99% after 100 cycles. The aforementioned literatures reveal that solid phase regeneration requires a high temperature above 650 °C, and additional Li_2CO_3 is needed to recover LFP. Low-temperature aqueous relithiation can be carried out under atmospheric pressure, but R-LFP still needs to be sintered at high temperature to restore its crystal structure. In addition, the current direct regeneration schemes of S-LFP are mostly based on the decommissioned batteries as raw materials, while less research has been conducted on the spent scraps produced in battery manufacturing. Thus, it is meaningful to develop a direct regeneration method without adding auxiliaries to recycle the S-LFP materials, and to investigate the mechanism of regeneration.

Herein, a direct regeneration scheme with low energy consumption and high economic value is developed. The S-LFP from spent scraps in battery manufacturing can be recovered by low-temperature sintering (550 °C) without adding extra lithium salts. Through revealing the evolution of structure, morphology, particle size and surface compositions of the S-LFP before and after direct regeneration, the mechanism of sintering regeneration is elucidated. This work paves a new way to recycle the S-LFP scraps from battery manufacturing, which is beneficial to establishing a better cycling loop for the LFP batteries.

2 Experimental

2.1 Regeneration process

The S-LFP powder obtained from spent scraps was kindly provided by Fujian Evergreen New Energy Technology Co., Ltd. (China). Without any pretreatment, the S-LFP was regenerated by solid phase sintering at 400, 450, 500, 550, and 600 °C for 3 h, and at 550 °C for 2, 3, and 4 h in a tube furnace (OTF−1200X, MTI Corporation) in the Ar atmosphere. For the sake of simplicity, the label of "R-Temperature-Time" is used to represent the corresponding sample, such as "R-550-3" represents that the R-LFP materials calcined at 550 °C for 3 h.

2.2 Material characterization

The variations of mass and heat flow of S-LFP sample with the temperature were measured by the simultaneous thermogravimetric analyzer (TG−DSC, STA300, Hitachi) from room temperature (RT) to 800 °C with a heating rate of 10 °C/min in the Ar atmosphere. To analyze the elemental concentration of S-LFP and R-LFP materials, both inductively coupled plasma optical emission spectrometer (ICP-OES, ICAP7400 radial, Thermo Fisher) and X-ray fluorescence spectrometer (XRF, XRF−1800, Shimadzu) measurements were performed. X-ray diffraction patterns were recorded within the scattering angle (2θ) range from 5° to 120° with a scan speed of 2 (°)/min by an X-ray

diffractometer (XRD, Rigaku-type, SmartLab) with monochromatic Cu K_α radiation. The crystal structural parameters of S-LFP and R-LFP were refined with the Rietveld method using FullProf software [19]. SEM images and EDS mapping were obtained by using a scanning electron microscope (SEM, JSM−7900F, JEOL) equipped with an energy-dispersive spectrometer (EDS), and the size distributions were statistically calculated by Nano Measurer software. TEM images and EDS mapping were obtained through the utilization of a high-resolution transmission electron microscopy (HR-TEM, Titan G2 60−300, FEI) equipped with an energy-dispersive spectrometer (EDS). The surface elemental compositions were determined by X-ray photoelectron spectroscopy (XPS, PHI VersaProbe 4, ULVAC-PHI) with monochromatic Al K_α radiation. Raman measurements (Raman, inVia, Renishaw) were utilized to characterize the carbon layer on the S-LFP and R-LFP samples using a 532 nm laser excitation.

2.3 Electrochemical measurements

To prepare the electrode, the active material, Super-P, and polyvinylidene fluoride (PVDF) with a mass ratio of 8:1:1 was dispersed in N-methyl-2-pyrrolidone (NMP) to form a homogeneous slurry. Then, the slurry was coated on a current collector (Al foil), followed by drying at 120 °C for 4 h to remove the NMP. Finally, the electrode was cut into pieces of 12 mm in diameter, and the mass loading of the electrode was 1.0−2.0 mg/cm^2. CR2025 coin cells were assembled in a glovebox with Ar atmosphere protection (H_2O and O_2 concentration less than 1×10^{-5} wt.%), with a metallic Li foil serving as the counter electrode, and Celgard 2325 as the separator. The electrolyte was 1 mol/L $LiPF_6$ dissolved in ethylene carbonate (EC) and diethyl carbonate (DEC) (1:1 in volume) solution.

The galvanostatic charge/discharge tests were conducted between 2.5 and 4.2 V (vs Li/Li$^+$) at 1*C* (170 mA/g) at room temperature ((25±0.5) °C) on the Neware battery test system. Cyclic voltammetry (CV) was performed on an electrochemical workstation (Squidstat Prime) in the potential window of 2.5−4.2 V at a scan rate of 0.1 mV/s. Electrochemical impedance spectroscopy (EIS) was performed on an electrochemical workstation (Interface 5000E, Gamry) using a voltage amplitude of 5 mV over the frequency range of 0.01−100000 Hz.

3 Results and discussion

3.1 Composition, thermal and structure characteristics

XRF results (Table 1) show that trace Ti and Al are introduced in the production of LFP by doping and mechanical crushing of S-LFP, respectively. This homogeneous introduction can potentially have a beneficial effect on the electrochemical performance of R-LFP [20,21]. ICP reveals that the molar ratio of Li, Fe and P is 1.014:1:1.026, implying no Li deficiency in S-LFP. Based on the above analysis, the regeneration strategy of one-step sintering without Li supplement is determined.

Table 1 XRF measurement of S-LFP (wt.%)

Li	Fe	P	O	Al	Ti
−	58.192	23.097	17.936	0.248	0.332

To determine the regeneration sintering temperature of S-LFP, TG−DSC measurement was carried out from RT to 800 °C with a heating rate of 10 °C/min in the Ar atmosphere. As shown in Fig. 1(a), the mass losses of S-LFP can mainly be divided into three steps, including the evaporation of adsorbed and crystal water (0.062%) below 150 °C in the first stage, the decomposition of PVDF (1.924%) in a temperature range of 150−500 °C in the second stage, and transformation of the crystal structure and surface composition (0.390%) in S-LFP in a temperature range of 500−800 °C in the third stage [22,23]. As previously reported [24], the decomposition products of PVDF contain carbon as well as fluorine-containing components, which can interact with S-LFP to form unique surface compositions and crystal structure that evolve further at higher temperatures. Therefore, the temperature of solid sintering regeneration is determined to be 400−600 °C.

XRD was utilized to follow the changes in crystalline phases during the sintering process. The diffraction patterns of S-LFP and R-LFP (Figs. 1(b, c)), which can be indexed to a primarily olivine-type structure of LFP (PDF# 81-1173), are comparable and free of $FePO_4$, and Fe_2O_3 residual peaks except for C peak. This result is consistent with the high Li content as determined by the ICP.

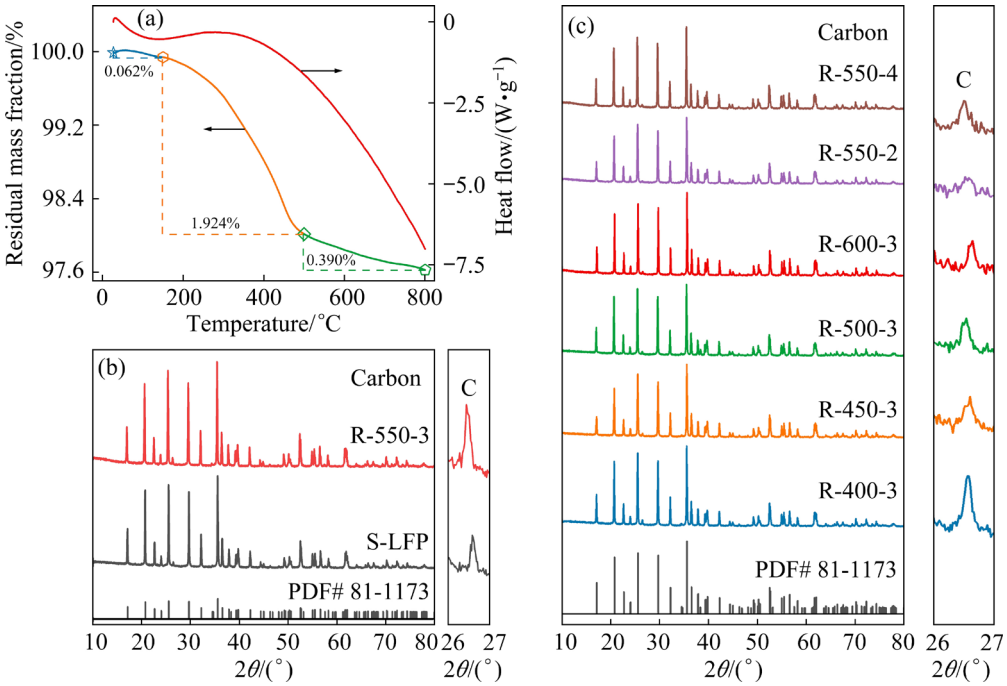

Fig. 1 TG−DSC curves of S-LFP tested in Ar atmosphere (a); XRD patterns of S-LFP and R-LFP samples (b, c)

Furthermore, the C peak of R-LFP is higher than that of S-LFP because of the decomposition of PVDF, especially for R-550-3, implying that a thicker carbon layer is formed on the surface of R-LFP after sintering.

Generally, Li^+ can only diffuse along the [010] direction in LFP structure as it only possesses a one-dimensional Li^+ diffusion channel, which can be blocked by the Fe atom because of the Li−Fe antisite defect (the exchange site of Fe atom and Li atom), leading to increased diffusion resistance of Li^+ [18,25]. Thus, the Li−Fe antisite defect is regarded as a major contributor to the electrochemical performance degradation of the LFP. To further explore the fine variations in crystal structure of LFP during regeneration, the S-LFP and R-LFP were refined by FullProf software (Fig. S1 in Supporting Information (SI)). The refinement was repeated three times for each sample.

As displayed in Tables S1−S9 in SI, it is interesting that the refinement results show that R-LFP contains a certain amount of F-doping in addition to the Li−Fe antisite defect. It is obvious that the Li−Fe antisite defect first decreases greatly from 5.73% to 1.20% and then slightly increases to 1.53% when regeneration temperature increases. In contrast, the F-doping content exhibits the opposite trend from the Li−Fe antisite defect (Fig. 2(a)). Moreover, The Li−Fe antisite defect gradually decreases with a longer regeneration time, whilst the F-doping content increases in the initial period and then decreases thereafter (Fig. 2(b)). These results reveal that F is doped to the O(2) site, and antisite defects can be repaired by using an appropriate temperature and holding time. In contrast, antisite defects are rarely repaired and few F atoms diffuse at low temperatures and short holding time because of insufficiently ionic diffusion driving force, whereas higher temperatures and longer holding time lead to an increase in antisite defects and the release of doping F atoms. Compared to the S-LFP sample with a high Li−Fe antisite defect of 5.73% (Fig. 2(c)), R-550-3 displays the lowest Li−Fe antisite defect (1.20%) and the highest F-doping content (1.93%) (Fig. 2(d)), suggesting the optimal Li^+ diffusion kinetics for R-550-3 as F-doping to the O(2) site can enhance the electron mobility of the olivine and Li^+ diffusion [24,26,27].

Raman results, as shown in Figs. 3(a, b), confirm that a carbon layer is formed by the decomposition of PVDF. In special, the peaks at ~1335 cm^{-1} (D band) and ~1585 cm^{-1} (G band) can be attributed to the disordered carbon and the ordered graphitic carbon, respectively [28]. Compared with S-LFP (I_D/I_G=0.28), R-LFP exhibits

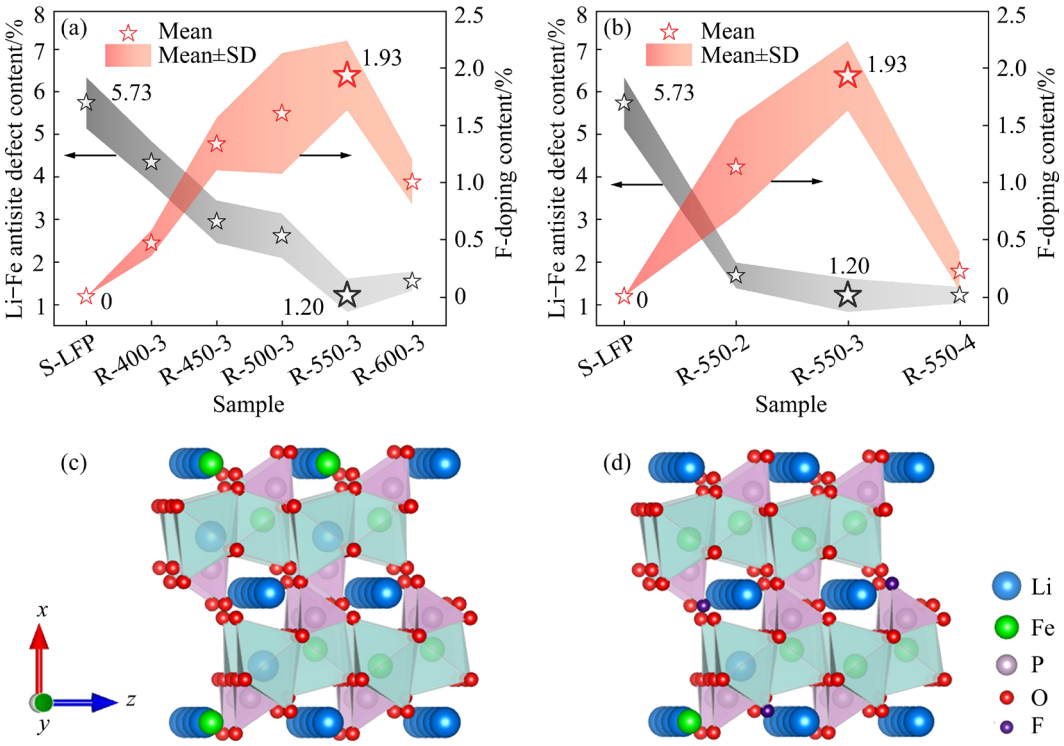

Fig. 2 Variations of Li−Fe antisite defect content and F-doping content of S-LFP and R-LFP samples at different temperatures (a) and time (b); Crystal structure of S-LFP (c) and R-550-3 (d) samples

a lower I_D/I_G value, and R-550-3 shows the minimum value of 0.19 (Figs. 3(c, d) and Table S10 in SI). This indicates that the decomposition of PVDF results in the formation of a more ordered carbon coating layer, which would be in favor of the increase of the electronic conductivity [29]. Moreover, ICP was carried out to determine the Li in the R-LFP after sintering regeneration. As shown in Fig. 3(e), the Li mass fraction in R-LFP gradually increases with increasing regeneration temperature and time. Specifically, the Li mass fraction in R-550-3 is 4.330%, which is higher than that of S-LFP (4.096%) (Table S11 in SI). The result highlights that higher regeneration temperature and longer regeneration time result in more thorough decomposition of PVDF impurities, while the Li element does not volatilize in the low-temperature sintering regeneration process.

3.2 Electrochemical performance

As shown in Figs. 4(a) and S2(b) in SI, the initial discharge capacities of R-LFP samples at 0.1*C* are all significantly increased as compared to S-LFP (148.0 mA·h/g), among which the R-550-3 shows the highest initial discharge capacity of 157.3 mA·h/g. This is because the lower Li−Fe antisite defect of R-LFP opens up the one-dimensional Li^+ diffusion channel, which can bring the electrochemically inactive Li back, leading to the recovery of redox active sites and the corresponding reversible capacity.

As shown in Figs. 4(b) and S2(c) in SI, the rate performances of S-LFP and R-LFP are further evaluated from 0.1*C* to 2*C* within the potential window of 2.5−4.2 V, and the initial charge−discharge profiles of S-LFP and R-550-3 at different rates are depicted in Fig. S2(a) in SI. R-550-3 exhibits the high discharge capacities of 147.7 and 138.2 mA·h/g at 1*C* and 2*C*, respectively, which are higher than those of S-LFP (133.8 and 124.7 mA·h/g) (Fig. 4(b)). The superior rate performance can be attributed to lower Li−Fe antisite defect, suitable F-doping, as well as ordered carbon coating layer, which enhance the electron mobility of the olivine, Li^+ diffusion kinetics, and electronic conductivity of electrode. Moreover, R-LFP exhibits enhanced rate performance except for R-400-3 (Fig. S2(c) in SI). This is because PVDF only partially decomposes at 400 °C. In addition to the rate capability measurements, the long-term cycling performance of S-LFP and R-LFP was investigated at 1*C*, as shown in Figs. 4(c)

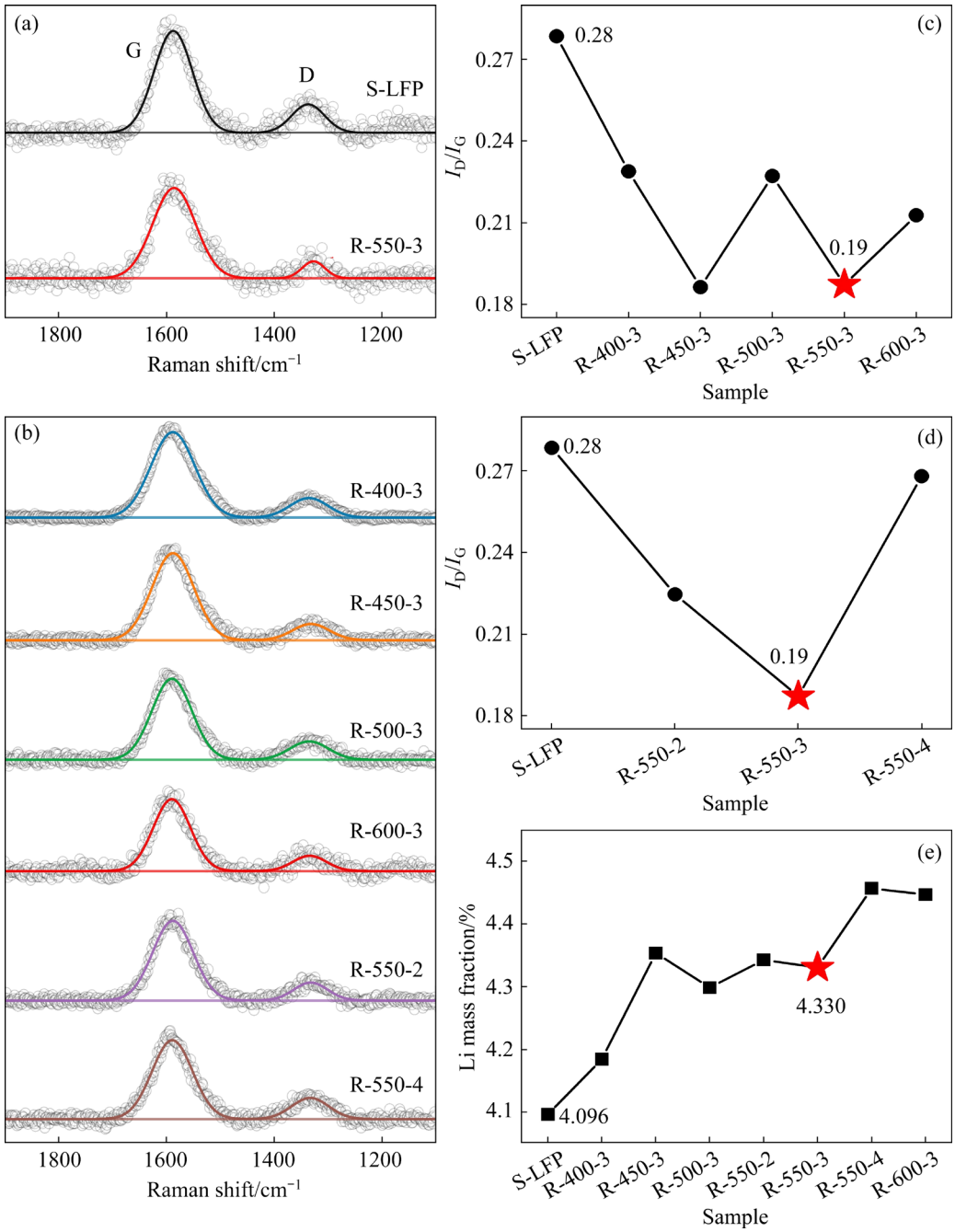

Fig. 3 Raman spectra of S-LFP and R-LFP samples (a, b); Variations of I_D/I_G of S-LFP and R-LFP samples at different temperatures (c) and time (d); Variations of Li mass fraction of S-LFP and R-LFP samples (e)

and S2(d) in SI. The capacity and coulombic efficiency of S-LFP declines rapidly after 100 cycles, and the discharge capacity is below 75 mA·h/g (Fig. 4(c)), suggesting the poor cyclic performance of S-LFP. Due to the damage of the structure and morphology without fully repairing, R-400-3 shows a discharge capacity of 63.9 mA·h/g after 500 cycles at 1*C*, with a capacity retention of 48 % (Fig. S2(d) in SI). Except for R-400-3 sample, the cyclic performance of R-LFP is enhanced. Specifically, the discharge capacity of R-550-3 remains at 133.2 mA·h/g after 500 cycles with a capacity retention of 92 %. These results reveal that R-LFP presents enhanced cyclic stability than S-LFP, especially for R-550-3, which is attributed to the fast-electronic conductivity of the ordered carbon network as well as the perfect olivine-type structure with lower Li−Fe antisite defect.

Cyclic voltammetry is a useful technique for the characterization of electrochemical reaction information of electrode materials. As shown in Figs. 5(a) and S3(a) in SI, R-550-3 presents the

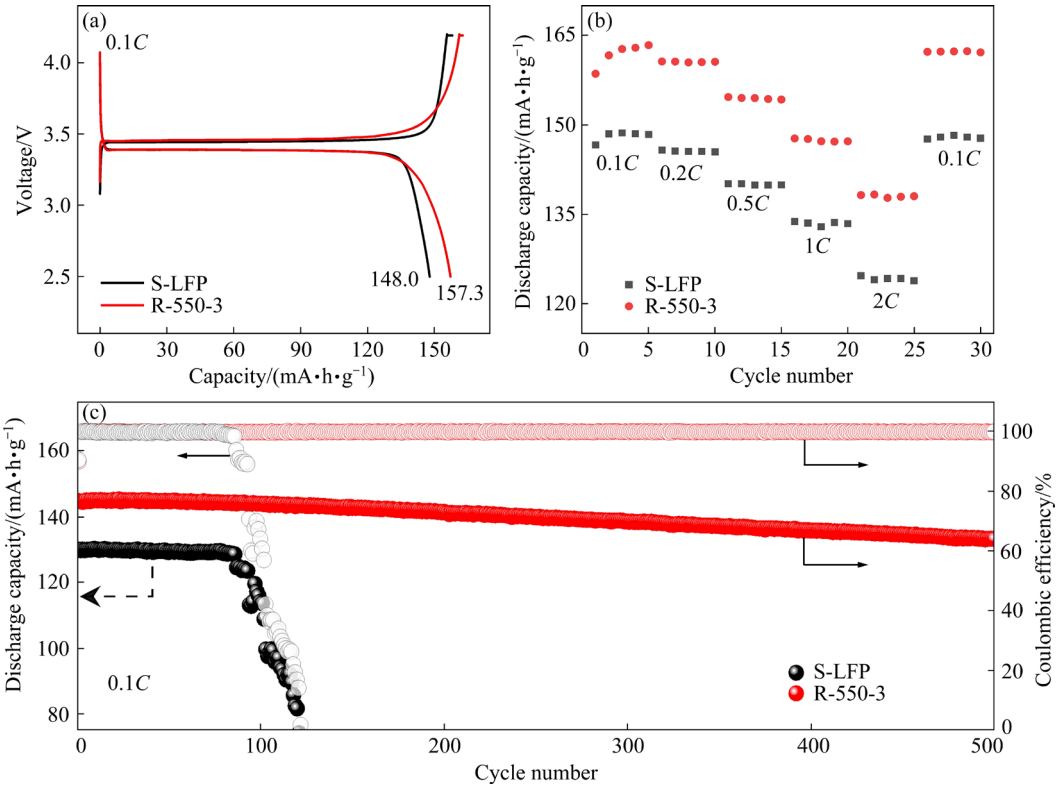

Fig. 4 Initial charge−discharge profiles in potential window of 2.5−4.2 V at 0.1*C* (a), rate performance from 0.1*C* to 2*C* (b) and cyclic performance at 1*C* (c) of S-LFP and R-550-3 samples

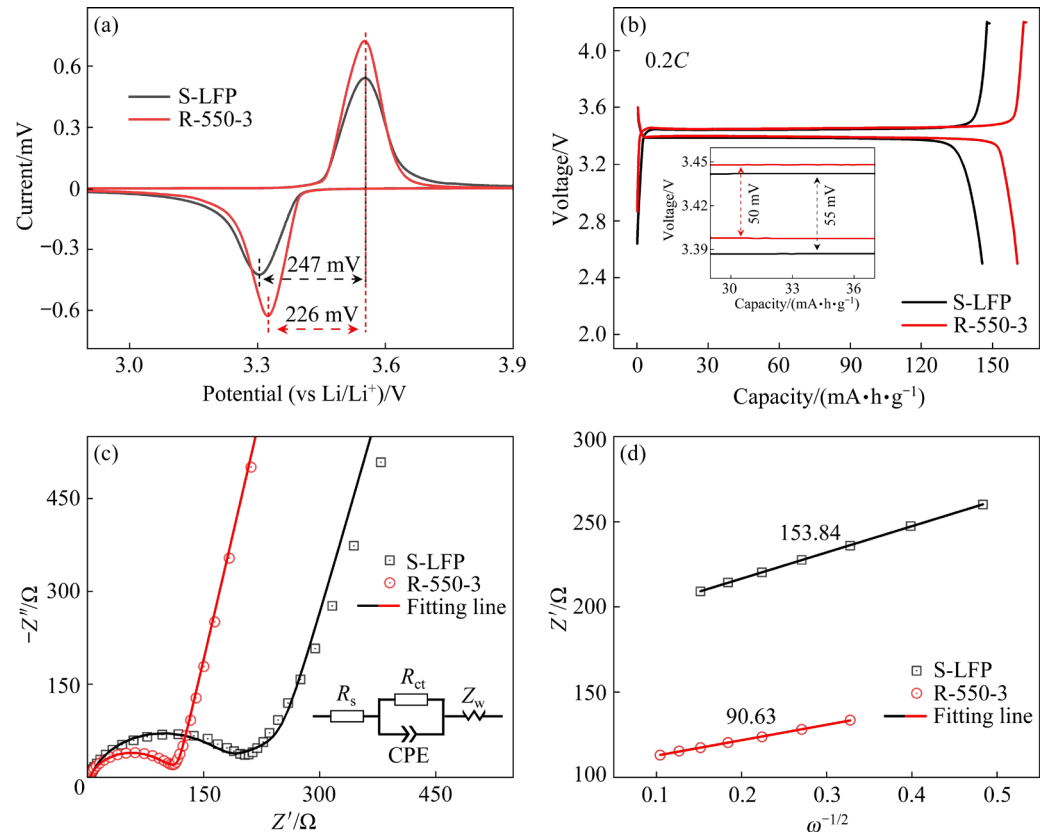

Fig. 5 Third cycle of CV plots at scan rate of 0.1 mV/s (a), charge−discharge profiles in potential region from 2.5 to 4.2 V at 0.2*C* (inset shows the magnified region of potential plateaus) (b), Nyquist, fitting curves and equivalent circuit plots (c), and fitting curves of Z' versus $\omega^{-1/2}$ (d) for S-LFP and R-550-3 samples

lowest overpotential (potential interval between the oxidation and reduction peaks) of 226 mV, whereas that of S-LFP is 247 mV. Moreover, R-550-3 displays a lower potential interval of 50 mV (Fig. 5(b)) between the charge and discharge plateaus, lower than that of S-LFP (55 mV). These results demonstrate that R-LFP exhibits smaller polarization, better reaction kinetics and reversibility, resulting an enhanced electrochemical performance.

To measure the Li^+ diffusion coefficient of S-LFP and R-LFP sample, the EIS tests were conducted, and the results are shown in Figs. 5(c) and S3(b) in SI. Normally, the Nyquist curves can be divided into three regions: the ohmic resistance (R_s) in the high-frequency region; the charge transfer resistance (R_{ct}) in medium-frequency semicircular region, which corresponds to the electrochemical reaction at the interface of electrode and electrolyte; the Warburg diffusion resistance (Z_w) in low-frequency linear region, which corresponds to the Li^+ diffusion inside the materials [30]. Obviously, the R-LFP exhibits a significantly reduced R_{ct} in comparison to S-LFP. Specifically, the R_{ct} initially decreases significantly from 161.20 to 94.45 Ω and subsequently increases slightly to 106.30 Ω with increasing regeneration temperature and time, where the minimum value is located at the R-550-3 spectra (Table S12 in SI). It is confirmed that the ordered carbon coating network formed by the decomposition of PVDF is the dominant effective factor in enhancing the interfacial electrochemical reactivity. Furthermore, the solid phase Li^+ diffusion coefficients (D_{Li^+}) are calculated by Eq. (1):

$$D_{Li^+}=R^2T^2/(2A^2n^4F^4C^2\sigma^2) \quad (1)$$

where R, T, A, n, F, C, and σ represent the molar gas constant (8.314 $J\cdot mol^{-1}\cdot K^{-1}$), thermodynamic temperature (298.15 K), electrode surface area (1.13 cm^2), number of electrons (n=1, Li^+), Faraday constant (96485 C/mol), concentration of Li^+ (7.69×10^{-3} mol/mL in this work) [31,32], and the Warburg coefficient, respectively.

σ can be calculated by Eq. (2), and the fitting curves of Z' versus $\omega^{-1/2}$ are shown in Figs. 5(d) and S3(c) in SI:

$$Z'=R_s+R_{ct}+\sigma\omega^{-1/2} \quad (2)$$

where Z' and ω represent the real impedance and angular frequency, respectively. The D_{Li^+} for R-550-3 (5.72×10^{-14} cm^2/s) is almost three times that of S-LFP (1.98×10^{-14} cm^2/s). The enhanced Li^+ diffusion coefficient and excellent reaction kinetics for R-LFP can be attributed to significant reduction of Li−Fe antisite defect, and the F-doping during the low-temperature sintering [26,33].

3.3 Morphology and surface chemistry characteristics

To further investigate the underlying reasons of the enhanced cyclic stability and reaction kinetics, XPS was utilized to measure the surface chemical composition and valence states. As presented in Fig. S4(a), Li, Fe, P, O, C, and F can be detected in the survey spectra of S-LFP, R-400-3, R-550-2, and R-550-3, but a far lower F 1s spectral signal on the R-LFP surface than on the S-LFP surface, suggesting the decomposition of PVDF during low-temperature sintering.

For C 1s spectra, the peaks at 284.8, 286.3, 288.9, and 290.9 eV can be assigned to the C—C, C═C, C—F, and —CF_2 bonds (Fig. 6(a)) [34,35]. The peak of —CF_2 can be observed in S-LFP, which comes from the PVDF binder in electrode. However, the peak intensity of —CF_2 decreases obviously for R-LFP owing to the decomposition of PVDF. It totally disappears in the R-550-2 and R-550-3 samples, indicating that the PVDF in S-LFP decomposes completely at 550 °C. As presented in Fig. 6(b), the F 1s spectra can be deconvoluted into three peaks at 688.3, 687.5, and 685.1 eV, attributing to —CF_2, C—F, and LiF, respectively [24,34,36].

Likewise, as observed in C 1s spectra, the peak of —CF_2 in F 1s spectra can only be detected in S-LFP and R-400-3 with a content of 64.14% and 35.14%, respectively. In addition, the C content in R-550-2 (46.3 at.%) and R-550-3 (46.49 at.%) sample is higher than that of S-LFP of 45.6 at.%, while the F content follows the reverse trend from the C content (Table 2). It is consistent with the analysis results from C 1s spectra that the PVDF has been transformed into carbon coating layer at 550 °C completely. Beyond that, in contrast to R-400-3, the stronger peaks of LiF peak for R-550-2 and R-550-3 can be observed in F 1s spectra, which is mainly derived from the decomposition of PVDF. Moreover, a higher content of LiF can be found on the surface of R-550-2 sample than on the surface of R-550-3,

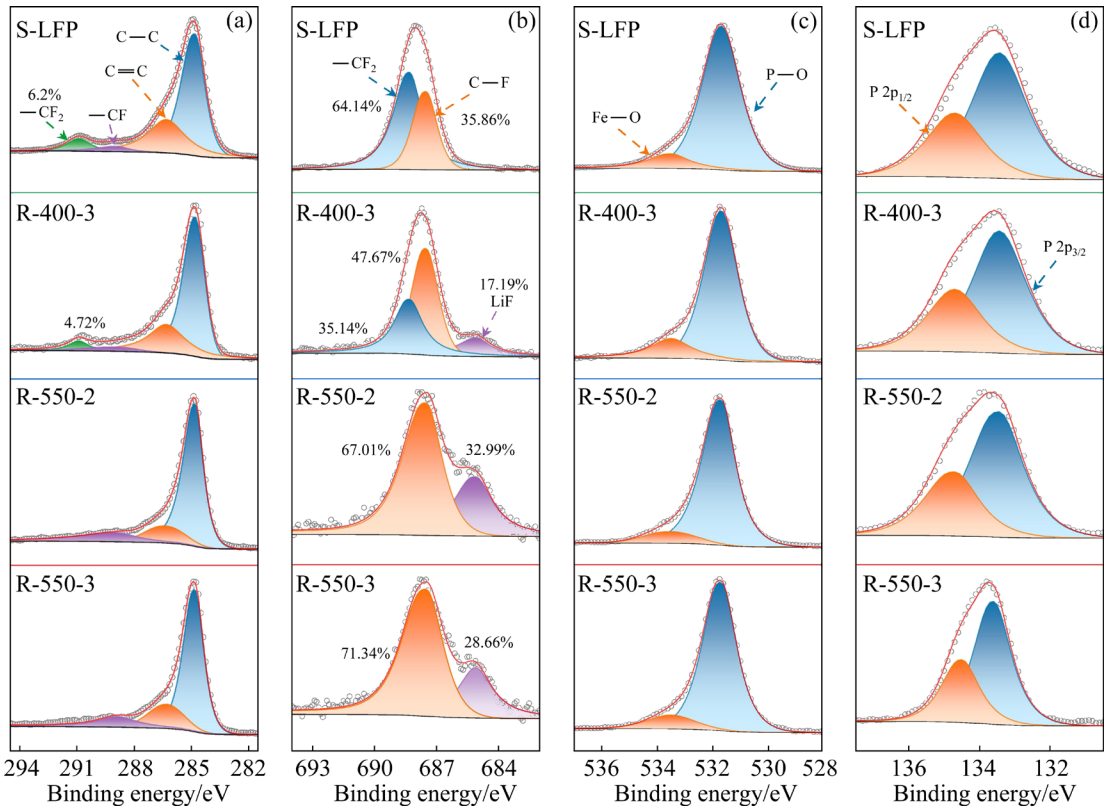

Fig. 6 XPS spectra of C 1s (a), F 1s (b), O 1s (c) and P 2p (d) for S-LFP, R-400-3, R-550-2, and R-550-3 samples

Table 2 Contents of C (at.%) and F (at.%) of S-LFP, R-400-3, R-550-2, R-550-3 based on XPS

Element	S-LFP	R-400-3	R-550-2	R-550-3
C	45.6	40.52	46.3	46.49
F	6.5	8.96	4.55	4.02

because the F in the LiF coating layer gradually diffuses into the interior of LFP to form the F-doping as regeneration time is extended to 3 h, which is in well accordance with the XRD refinement results (Fig. 2(b)). In short, a LiF protective layer, one of the primary components of cathode electrolyte interphase (CEI) [37], attributed to the decomposition of PVDF, is formed on the surface of R-LFP, which can mitigate the occurrence of side reactions between LFP and electrolyte.

Due to spin−orbit coupling, the peaks of Fe 2p spectra (Fig. S4(b) in SI) are split into Fe $2p_{3/2}$ and Fe $2p_{1/2}$, with Fe $2p_{3/2}$ emerging at 710.5 eV and 712.5 eV for Fe(II) and Fe(III), respectively [38,39]. As shown in Fig. S4(b) in SI, the main Fe $2p_{3/2}$ peak of R-LFP (710.75 eV) shifts toward a lower binding energy than that of S-LFP (711.75 eV), indicating the lower valence state of Fe and the recovery of crystal structure in R-LFP through low-temperature sintering. In addition, the four samples do not show obvious differences in O 1s, P 2p and Li 1s spectra. In detail, the peaks of Fe—O and P—O are observed at 533.5 and 531.7 eV, which correspond to the FeO_6 octahedron and PO_4 tetrahedron in the orthorhombic olivine structure, respectively (Fig. 6(c)) [35]. The peak at 55.3 eV can be attributed to Li—O, and the peaks at 133.6 eV and 134.5 eV can be attributed to P $2p_{3/2}$ and P $2p_{1/2}$, respectively, in the LFP structure (Figs. 6(d) and S4(c) in SI) [33,35,40].

To better observe the coating layer of C and LiF on the R-LFP surface, the surface morphology was investigated by SEM and TEM. The secondary particle with a maximum diameter of 18 μm is observed in S-LFP because of serious aggregation caused by the PVDF binder, which is significantly reduced in R-LFP samples (Fig. S5 in SI). In addition, particle size distributions (Figs. S5(g, h) in SI) were obtained by counting 40 and 100 secondary particles, respectively. The D_{10}, D_{50}, and D_{90} of R-550-3 are calculated to be 1.3, 2.3 and 3.7 μm, respectively, which are lower than those of

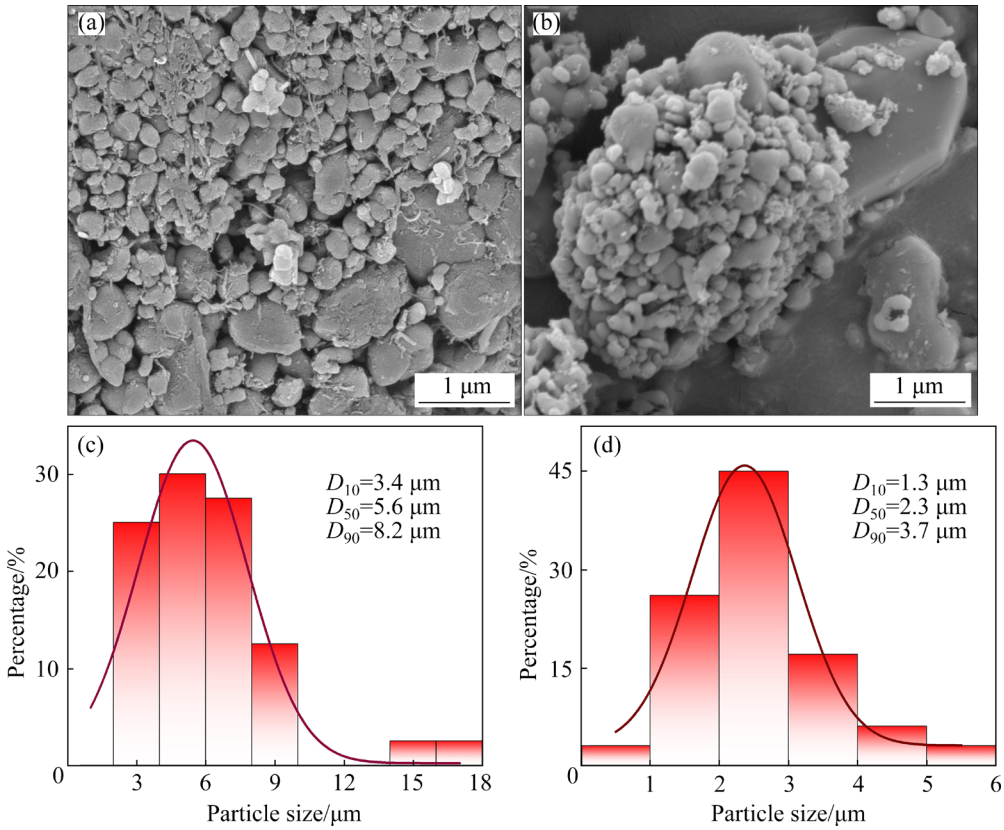

Fig. 7 SEM images (a, b) and particle size distribution obtained from SEM images by Nano Measurer software (c, d) of S-LFP (a, c) and R-550-3 (b, d) samples

S-LFP (3.4, 5.6, and 8.2 μm, Figs. 7(c, d)). These results reveal that the finer and more narrower particle size distribution of R-LFP can shorten the Li^+ diffusion path for bulk reaction, resulting in superior reaction kinetics.

Furthermore, a smooth surface of the secondary particle can be observed in R-550-3 (Fig. 7(b)) as compared to S-LFP (Fig. 7(a)), implying a layer comprised of C and LiF on the surface of R-550-3, which can be directly confirmed by TEM. As shown in the HR-TEM image of S-LFP (Fig. 8(a)), the interplanar spacing in Region I (5d=1.228 nm) is consistent with the (121) crystal plane of orthorhombic olivine-type LFP (Fig. 8(b)). And the surface of S-LFP nano-particles is coated with a very thin amorphous carbon layer of ~2 nm as well as residual PVDF. As depicted in Fig. 8(d), the interplanar spacing in Region III (5d=1.727 nm) agrees well with (111) or (201) crystal plane of LFP (Fig. 8(e)), and a thicker amorphous carbon layer of ~5 nm can be observed on the surface of R-550-3. In addition, the outer surface of the carbon layer exhibits uniform interplanar spacings (5d=1.03 nm), corresponding to the (200) crystal plane of LiF (Fig. 8f). These results reveal that the surface of R-550-3 is uniformly coated with a thicker carbon layer and a LiF layer, forming a conductive network structure, in agreement with the XPS analyses (Figs. 6(a, b)). Furthermore, EDS mapping demonstrates a homogeneous distribution of elements, while the F intensity registered in R-550-3 is weaker than that of S-LFP (Figs. 8(c, g) and S6 in SI). This indicates that homogeneous LiF layer and F doping are successfully introduced into the R-550-3 because of the decomposition of PVDF.

4 Conclusions

(1) An efficient low-temperature sintering regeneration method for restoring the electro-chemical performance of spent $LiFePO_4$ (S-LFP) scraps is proposed.

(2) After calcining at 550 °C for 3 h in Ar atmosphere, the Li−Fe antisite defect of S-LFP is reduced, and a carbon coating layer mixing with LiF derived from the decomposition of PVDF is formed. Moreover, regenerated $LiFePO_4$ (R-LFP)

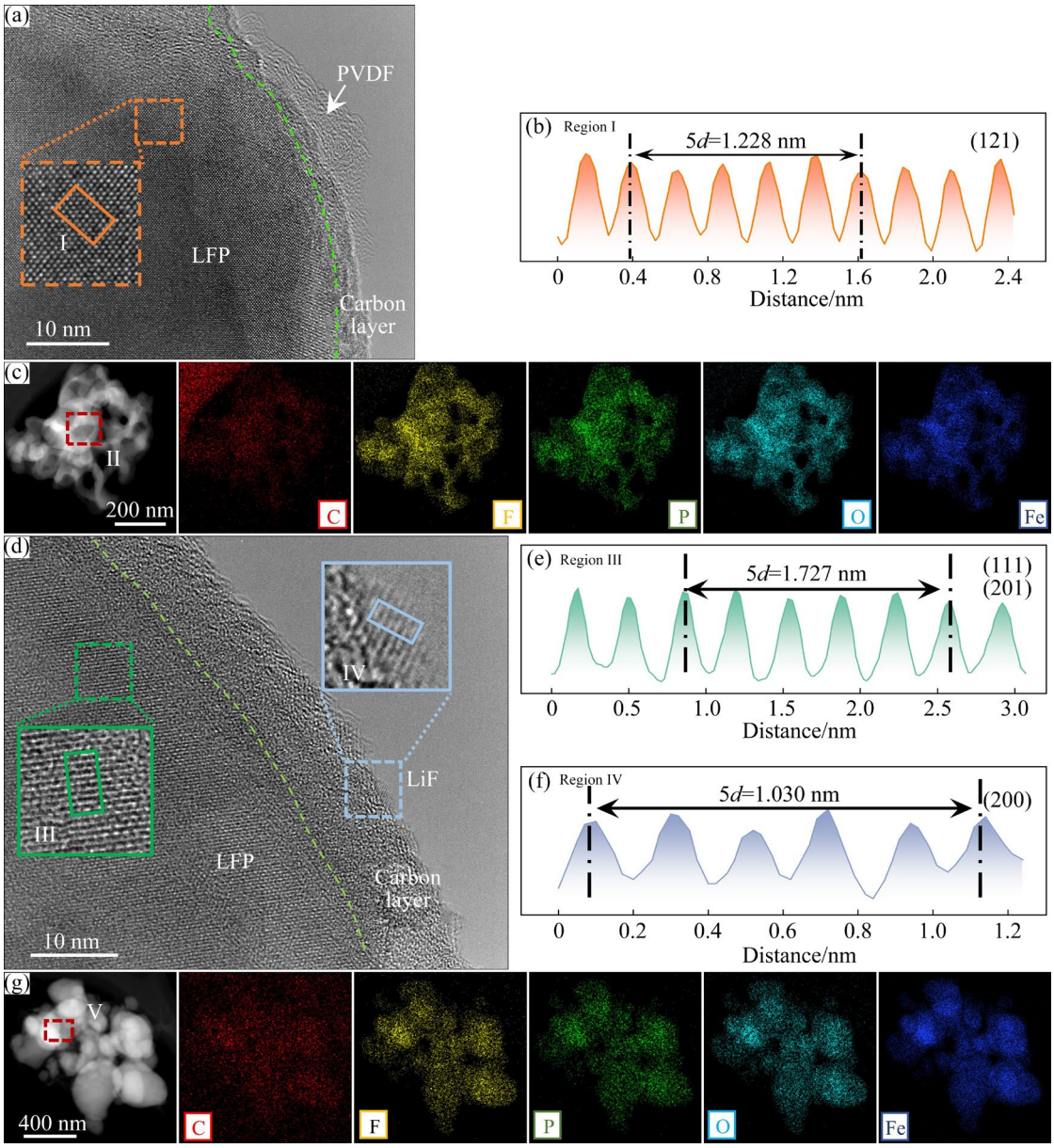

Fig. 8 HR-TEM images (a, d), Interplanar spacings of corresponding areas (b, e, f), and EDS mapping images (c, g) of S-LFP (a−c) and R-550-3 (d−g) samples

sample exhibits the finer and more homogeneous secondary particle size.

(3) R-LFP exhibits smaller polarization, better reaction kinetics and reversibility. Thus, the R-LFP sample at 550 °C for 3 h delivers a high discharge capacity of 157.3 mA·h/g at 0.1*C* and maintains 92% of its initial capacity after 500 cycles at 1*C*.

(4) This work paves a new way to recycle the S-LFP scraps from battery manufacturing, which is a more environmentally friendly and higher economic value solution compared with hydrometallurgical and pyrometallurgical methods.

CRediT authorship contribution statement

Hong-lei SONG: Methodology, Validation, Data curation, Writing − Original draft; **Zhi-xing WANG:** Data curation, Writing – Review & editing; **Xin-hai LI:** Funding acquisition; **Hua-jun GUO:** Visualization, Supervision; **Wen-jie PENG:** Supervision, Funding acquisition; **Zhi-liang YAN:** Visualization; **Cheng-hui ZHENG:** Visualization, Funding acquisition; **Jian-qiu LI:** Investigation; **Jie-xi WANG:** Formal analysis; **Guo-chun YAN:** Methodology, Validation, Supervision, Writing − Review & editing.

Declaration of competing interest

The authors declare that they have no known

competing financial interests or personal relationships that could have appeared to influence the work reported in this paper.

Acknowledgments

This work was supported by the National Natural Science Foundation of China (Nos. 51874360, 51974370, 52074360, 52122407, 52174285), the Innovation and Entrepreneurship Project of Hunan Province, China (No. 2020GK4051), the Key R&D Program of Yunan Province, China (No. 202103AA080019), and the Natural Science Foundation for Distinguished Young Scholars of Hunan Province, China (No. 2024JJ2077).

Supporting Information

The Supporting Information in this paper can be found at: http://tnmsc.csu.edu.cn/download/21-p2421-2023-1336-Supporting_Information.pdf.

References

[1] LI Jian-lin, FLEETWOOD J, HAWLEY W B, KAYS W. From materials to cell: State-of-the-art and prospective technologies for lithium-ion battery electrode processing [J]. Chemical Reviews, 2022, 122(1): 903−956.

[2] ZUBI G, DUFO-LOPE R, CARVALHO M, PASAOGLU G. The lithium-ion battery: State of the art and future perspectives [J]. Renewable & Sustainable Energy Reviews, 2018, 89: 292−308.

[3] ZHOU Tao, XIE Ling-ling, NIU Yu, XIAO Hao-ran, LI Yu-jie, HAN Qing, QIU Xue-jing, YANG Xin-li, WU Xian-yong, ZHU Li-min, PANG Huan, CAO Xiao-yu. New insights on $(V_{10}O_{28})^{6-}$-based electrode materials for energy storage: A brief review [J]. Rare Metals, 2023, 42(5): 1431−1445.

[4] GUAN Jian-ru, LIU Min-lu, ZHU Li-min, WANG Jia-mei, HAN Qing, YANG Xiao-xia, HUA Wei-bo, XIE Ling-ling, CAO Xiao-yu. Ni/Co bimetallic organic frameworks nanospheres for high-performance electrochemical energy storage [J]. Nano Research, 2024, 12(19): 10685−10692.

[5] ZHANG Ming-jun, WANG Li-fan, WANG Shi-qi, MA Tian-yi, JIA Fei-fei, ZHAN Chun. A critical review on the recycling strategy of lithium iron phosphate from electric vehicles [J]. Small Methods, 2023, 7(7): 2300125.

[6] SHEN Gao-yang, LI Bing-chuan, XU Yong-yi, CHEN Xi-zhuo, Katiyar S, ZHU Li-min, XIE Ling-ling, HAN Qing, QIU Xue-jing, WU Xian-yong, CAO Xiao-yu. Waste biomass garlic stem-derived porous carbon materials as high-capacity and long-cycling anode for lithium/sodium-ion batteries [J]. Journal of Colloid and Interface Science, 2024, 653: 1588−1599.

[7] LAI Xin, HUANG Yun-feng, DENG Cong, GU Huang-hui, HAN Xue-bing, ZHENG Yue-jiu, OUYANG Ming-gao. Sorting, regrouping, and echelon utilization of the large-scale retired lithium batteries: A critical review [J]. Renewable and Sustainable Energy Reviews, 2021, 146: 111162.

[8] QU Xin, ZHANG Bei-lei, ZHAO Jing-jing, QIU Bao-long, CHEN Xiang, ZHOU Feng-yin, LI Xiang-yun, GAO Shuai-bo, WANG Di-hua, YIN Hua-yi. Salt-thermal methods for recycling and regenerating spent lithium-ion batteries: A review [J]. Green Chemistry, 2023, 25(8): 2992−3015.

[9] SONG Yi-fan, XIE Bo-yi, SONG Shao-le, LEI Shu-ya, SUN Wei, XU Rui, YANG Yue. Regeneration of $LiFePO_4$ from spent lithium-ion batteries via a facile process featuring acid leaching and hydrothermal synthesis [J]. Green Chemistry, 2021, 23(11): 3963−3971.

[10] WANG Yu-qing, AN Ning, WEN Lei, WANG Lei, JIANG Xiao-tong, HOU Feng, YIN Yu-xin, LIANG Ji. Recent progress on the recycling technology of Li-ion batteries [J]. Journal of Energy Chemistry, 2021, 55: 391−419.

[11] KUMA J, NEIBER R R, PARK J, SOOMRO R A, GREENE G W, MAZARI S A, SEO H Y, LEE J H, SHON M, CHANG D W, CHO K Y. Recent progress in sustainable recycling of $LiFePO_4$-type lithium-ion batteries: Strategies for highly selective lithium recovery [J]. Chemical Engineering Journal, 2022, 431: 133993.

[12] WU De-you, WANG Dong-xing, LIU Zhi-qiang, RAO Shuai, ZHANG Kui-fang. Selective recovery of lithium from spent lithium iron phosphate batteries using oxidation pressure sulfuric acid leaching system [J]. Transactions of Nonferrous Metals Society of China, 2022, 32(6): 2071−2079.

[13] LI Fang-cheng, ZHANG Gang, ZHANG Zong-liang, YANG Jian, LIU Fang-yang, JIA Ming, JIANG Liang-xing. Regeneration of Al-doped $LiNi_{0.5}Co_{0.2}Mn_{0.3}O_2$ cathode material by simulated hydrometallurgy leachate of spent lithium-ion batteries [J]. Transactions of Nonferrous Metals Society of China, 2022, 32(2): 593−603.

[14] LI Peng-wei, LUO Shao-hua, ZHANG Lin, LIU Qiu-yue, WANG Yi-kai, LIN Yi-cheng, XU Can, GUO Jia, CHEALI P, XIA Xiao-ning. Progress, challenges, and prospects of spent lithium-ion batteries recycling: A review [J]. Journal of Energy Chemistry, 2024, 89: 144−171.

[15] LI Peng-wei, LUO Shao-hua, SU Fa-xian, ZHANG Lin, YAN Sheng-xue, LEI Xue-fei, MU Wen-ning, WANG Qing, ZHANG Ya-hui, LIU Xin, HOU Peng-qing. Optimization of synergistic leaching of valuable metals from spent lithium-ion batteries by the sulfuric acid-malonic acid system using response surface methodology [J]. Acs Applied Materials & Interfaces, 2022, 14(9): 11359−11374.

[16] WANG Chen-yan, QIU Xue-jing, SHEN Gao-yang, CHEN Xi-zhuo, WANG Jia-mei, XIE Ling-ling, HAN Qing, ZHU Li-min, LI Jing-jing, CAO Xiao-yu. Driving the rapid regeneration of $LiFePO_4$ from spent lithium-ion batteries through one-pot mechanochemical activation [J]. Green Chemistry, 2024, 26(3): 1501−1510.

[17] LI Xue-lei, ZHANG Jin, SONG Da-wei, SONG Ji-shun, ZHANG Lian-qi. Direct regeneration of recycled cathode material mixture from scrapped $LiFePO_4$ batteries [J]. Journal of Power Sources, 2017, 345: 78−84.

[18] XU Pan-pan, DAI Qiang, GAO Hong-peng, LIU Hao-dong, ZHANG Ming-hao, LI Ming-qian, CHEN Yan, AN Ke, MENG Ying shirley, LIU Ping, LI Yan-ran, SPANGENBERGER J S, GAINES L, LU Jun, CHEN Zheng. Efficient direct recycling of lithium-ion battery cathodes by

targeted healing [J]. Joule, 2020, 4(12): 2609−2626.

[19] RODRÍGUEZ-CARVAJAL J. Recent advances in magnetic structure determination by neutron powder diffraction [J]. Physica B: Condensed Matter, 1993, 192(1): 55−69.

[20] WANG Li-hua, LI Jian, ZHOU Hong-ming, HUANG Zu-qiong, TAO Sheng-dong, ZHAI Bing-kun, LIU Liang-qin, HU Le-shan. Regeneration cathode material mixture from spent lithium iron phosphate batteries [J]. Journal of Materials Science−Materials in Electronics, 2018, 29(11): 9283−9290.

[21] YANG Mu-rong, KE Wei-hsin. The doping effect on the electrochemical properties of $LiFe_{0.95}M_{0.05}PO_4$ ($M=Mg^{2+}$, Ni^{2+}, Al^{3+}, or V^{3+}) as cathode materials for lithium-ion cells [J]. Journal of the Electrochemical Society, 2008, 155(10): A729−A732.

[22] SONG Da-wei, WANG Xiao-qing, NIE He-he, SHI Hua, WANG Dong-ge, GUO Fen-xia, SHI Xi-xi, ZHANG Lian-qi. Heat treatment of $LiCoO_2$ recovered from cathode scraps with solvent method [J]. Journal of Power Sources, 2014, 249: 137−141.

[23] JING Qian-kun, ZHANG Jia-liang, LIU Yu-bo, ZHANG Wen-juan, CHEN Yong-qiang, WANG Cheng-yan. Direct regeneration of spent $LiFePO_4$ cathode material by a green and efficient one-step hydrothermal method [J]. Acs Sustainable Chemistry & Engineering, 2020, 8(48): 17622−17628.

[24] WANG Xu-feng, FENG Zhi-jun, HOU Xiao-long, LIU Ling-ling, HE Min, HE Xiao-shu, HUANG Jun-tong, WEN Zhen-hai. Fluorine doped carbon coating of $LiFePO_4$ as a cathode material for lithium-ion batteries [J]. Chemical Engineering Journal, 2020, 379: 122371.

[25] LI Zheng, HE Li-hua, ZHU Yun-fei, YANG Chao. A green and cost-effective method for production of LiOH from spent $LiFePO_4$ [J]. Acs Sustainable Chemistry & Engineering, 2020, 8(42): 15915−15926.

[26] MILOVIĆ M, JUGOVIĆ D, CVJETIĆANIN N, USKOKOVIĆ D, MILOŠEVIĆ A S, POPOVIĆ Z S, VUKAJLOVIĆ F R. Crystal structure analysis and first principle investigation of F doping in $LiFePO_4$ [J]. Journal of Power Sources, 2013, 241: 70−79.

[27] MENG Yan-shuang, LI Yu-zhu, XIA Jun, HU Qian-ru, KE Xin-you, REN Guo-feng, ZHU Fu-liang. F-doped $LiFePO_4$@N/B/F-doped carbon as high performance cathode materials for Li-ion batteries [J]. Applied Surface Science, 2019, 476: 761−768.

[28] LI Wei, ZHOU Min, LI Hao-miao, WANG Kang-li, CHENG Shi-jie, JIANG Kai. A high performance sulfur-doped disordered carbon anode for sodium ion batteries [J]. Energy & Environmental Science, 2015, 8(10): 2916−2921.

[29] WU Xing-long, GUO Yu-guo, SU Jing, XIONG Jun-wei, ZHANG Ya-li, WAN Li-jun. Carbon-nanotube-decorated nano-$LiFePO_4$@C cathode material with superior high-rate and low-temperature performances for lithium-ion batteries [J]. Advanced Energy Materials, 2013, 3(9): 1155−1160.

[30] WANG Xu-feng, FENG Zhi-jun, HUANG Jun-tong, DENG Wen, LI Xi-bao, ZHANG Hua-sen, WEN Zhen-hai. Graphene-decorated carbon-coated $LiFePO_4$ nanospheres as a high-performance cathode material for lithium-ion batteries [J]. Carbon, 2018, 127: 149−157.

[31] CHEN Ming, SHAO Leng-leng, YANG Hua-bin, REN Tie-zhen, DU Gao-hui, YUAN Zhong-yong. Vanadium-doping of $LiFePO_4$/carbon composite cathode materials synthesized with organophosphorus source [J]. Electrochimica Acta, 2015, 167: 278−286.

[32] TIAN Xiao-hui, ZHOU Ying-ke, WU Guan, WANG Peng-cheng, CHEN Jian. Controllable synthesis of porous $LiFePO_4$ for tunable electrochemical Li-insertion performance [J]. Electrochimica Acta, 2017, 229: 316−324.

[33] ZOU Yi-hui, CHEN Shuai, YANG Xian-feng, MA Na, XIA Yan-zhi, YANG Dong-jiang, GUO Shao-jun. Suppressing Fe-Li antisite defects in $LiFePO_4$/carbon hybrid microtube to enhance the lithium ion storage [J]. Advanced Energy Materials, 2016, 6(24): 1601549.

[34] JIN Ying-min, ZONG Xin, ZHANG Xue-bai, LIU Chao-jun, LI Dong, JIA Zheng-gang, LI Gen, ZHOU Xuan-guang, WEI Jun-hua, XIONG Yue-ping. Interface regulation enabling three-dimensional $Li_{1.3}Al_{0.3}Ti_{1.7}(PO_4)_3$-reinforced composite solid electrolyte for high-performance lithium batteries [J]. Journal of Power Sources, 2021, 501: 230027.

[35] JI Guan-jun, OU Xing, ZHAO Rui-rui, ZHANG Jia-feng, ZOU Jing-tian, LI Peng-fei, PENG De-zhao, YE Long, ZHANG Bao, HE Di. Efficient utilization of scrapped $LiFePO_4$ battery for novel synthesis of $Fe_2P_2O_7$/C as candidate anode materials [J]. Resources Conservation and Recycling, 2021, 174: 105802.

[36] HUO Han-yu, LI Xiao-na, CHEN Yue, LIANG Jian-neng, DENG Si-xu, GAO Xue-jie, DOYLE-DAVIS K, LI Ru-ying, GUO Xiang-xin, SHEN Yang, NAN Ce-wen, SUN Xue-liang. Bifunctional composite separator with a solid-state-battery strategy for dendrite-free lithium metal batteries [J]. Energy Storage Materials, 2020, 29: 361−366.

[37] ZHANG Jie-nan, LI Qing-hao, WANG Yi, ZHENG Jie-yun, YU Xi-qian, LI Hong. Dynamic evolution of cathode electrolyte interphase (CEI) on high voltage $LiCoO_2$ cathode and its interaction with Li anode [J]. Energy Storage Materials, 2018, 14: 1−7.

[38] ZHANG Jia-liang, HU Jun-tao, LIU Yu-bo, JING Qian-kun, YANG Cheng, CHEN Yong-qiang, WANG Cheng-yan. Sustainable and facile method for the selective recovery of lithium from cathode scrap of spent $LiFePO_4$ batteries [J]. Acs Sustainable Chemistry & Engineering, 2019, 7(6): 5626−5631.

[39] CASTRO L, DEDRYVÈRE R, El KHALIFI M, LIPPENS P E, BRÉGER J, TESSIER C, GONBEAU D. The spin-polarized electronic structure of $LiFePO_4$ and $FePO_4$ evidenced by in-lab XPS [J]. The Journal of Physical Chemistry C, 2010, 114(41): 17995−18000.

[40] RAMANA C V, AIT-SALAH A, UTSUNOMIYA S, MORHANGE J F, MAUGER A, GENDRON F, JULIEN C M. Spectroscopic and chemical imaging analysis of lithium iron triphosphate [J]. The Journal of Physical Chemistry C, 2007, 111(2): 1049−1054.

废旧 $LiFePO_4$ 的低温烧结高效直接再生

宋宏磊[1,2]，王志兴[1,2,3]，李新海[1,2,3]，郭华军[1,2,3]，彭文杰[1,2]，
颜志梁[4]，郑承辉[4]，李建球[4]，王接喜[1,2,3]，颜果春[1,2,3]

1. 中南大学 冶金与环境学院，长沙 410083；
2. 中南大学 教育部先进电池材料工程研究中心，长沙 410083；
3. 中南大学 湖南省有色金属增值冶金重点实验室，长沙 410083；
4. 福建常青新能源科技有限公司，龙岩 364200

摘　要：采用一步低温固相烧结法，实现了对废旧磷酸铁锂(S-LFP)形貌、晶体结构和电化学性能的直接修复。其中 550 ℃下烧结 3 h 再生的磷酸铁锂(R-LFP)的二次粒径分布更集中，D_{50} 由 5.6 μm 降为 2.3 μm；Li−Fe 反位缺陷含量从 5.73%降为 1.20%，并且实现了 F 对 O(2)位的掺杂；另外，由于 PVDF 的分解，在 R-LFP 表面形成了 C 和 LiF 的共包覆层。因此，R-LFP 表现出优异的 Li^+扩散动力学和导电性，在 0.1*C* 下具有 157.3 mA·h/g 的高放电比容量，1*C* 循环 500 次后仍具有 92%的容量保持率。

关键词：废旧磷酸铁锂；低温烧结；直接再生；高值化回收

(Edited by Bing YANG)